JGR Solid Earth

RESEARCH ARTICLE
10.1029/2019JB018935

Detection Limits and Near-Field Ground Motions of Fast and Slow Earthquakes

Grzegorz Kwiatek[1,2] and **Yehuda Ben-Zion**[3]

[1]Section 4.2: Geomechanics and Scientific Drilling, Helmholtz Centre Potsdam, GFZ German Research Centre for Geosciences, Potsdam, Germany, [2]Department of Earth Sciences, Institute of Geological Sciences, Free University Berlin, Berlin, Germany, [3]Department of Earth Sciences, University of Southern California, Los Angeles, CA, USA

Key Points:
- Several source characteristics influence limits to earthquakes detection and ground motion amplitudes at short epicentral distances
- Slip rise time, rupture velocity, and stress drop affect significantly the amplitude of seismic motion for a given event magnitude
- The shape of ground motion at short epicentral distance is governed primarily by radiation pattern and rupture directivity

Supporting Information:
- Supporting Information S1

Correspondence to:
G. Kwiatek,
kwiatek@gfz-potsdam.de

Citation:
Kwiatek, G., & Ben-Zion, Y. (2020). Detection limits and near-field ground motions of fast and slow earthquakes. *Journal of Geophysical Research: Solid Earth*, *125*, e2019JB018935. https://doi.org/10.1029/2019JB018935

Received 21 OCT 2019
Accepted 8 JUN 2020
Accepted article online 13 JUN 2020

Abstract We investigate theoretical limits to detection of fast and slow seismic events, and spatial variations of ground motion expected from *M* 6 earthquakes at short epicentral distances. The analyses are based on synthetic velocity seismograms calculated with the discrete wavenumber method assuming seismic velocities and attenuation properties of the crust in Southern California. The examined source properties include different magnitudes (*M* −1.0 to *M* 6.0), static stress drops (0.1–10 MPa), and slow and fast ruptures (0.1–0.9 of shear wave velocity). For the *M* 6 events we also consider variations in rise times producing crack- and pulse-type events and different rupture directivities. Slow events produce ground motion with considerably lower amplitude than corresponding regular fast earthquakes with the same magnitude, and hence are significantly more difficult to detect. The static stress drop and slip rise time also affect the maximum radiated seismic motion, and hence event detectability. Apart from geometrical factors, the saturation and depletion of seismic ground motion at short epicentral distances stem from radiation pattern, earthquake size (magnitude, stress drop), and rupture directivity. The rupture velocity, rise time, and directivity affect significantly the spatial pattern of the ground motions. The results can help optimizing detection of slow and fast small earthquakes and understand the spatial distribution of ground motion generated by large events.

1. Introduction

In the last two decades, significant progress in acquisition of seismic and geodetic data, coupled with improved analysis techniques and computing power, have led to detection of very small earthquakes, nonvolcanic tremor, and slow slip events (e.g., Dragert et al., 2004; Obara, 2002; Ross et al., 2019; Shelly et al., 2007). The use of machine learning techniques can improve further considerably the detection of minute fault motion events (e.g., Bergen et al., 2019; Kong et al., 2018). The increasing focus on very small events requires analysis of weak ground motion that is essentially at the noise level. However, weak ground motion with properties similar to earthquakes and tremor is dominated locally by cars, trains, air traffic, wind-shaking obstacles above the ground, and other nontectonic sources (Inbal et al., 2018; Johnson et al., 2019; Meng & Ben-Zion, 2018a; Riahi & Gerstoft, 2015). Theoretical constraints on plausible properties of motion generated by different types of slip events on faults at different source-receiver configurations can help separating tectonic from other sources of weak ground motion. This can be especially useful for automated techniques that process vast data sets and do not include validation of the nature of the detected sources.

Kwiatek and Ben-Zion (2016) conducted a theoretical parameter-space study on attenuation of amplitudes and spectral characteristics of motion generated by earthquakes with different magnitudes, various fast (subshear) rupture velocities and various stress drops. The wave propagation calculations used homogeneous solids with different seismic velocities and attenuation coefficients. In the present paper we generalize that study by considering also slow rupture velocities, variety of slip velocities, and more realistic crustal structures having depth-varying seismic properties. In addition to detection, the attenuation of amplitudes with distance from seismic sources is highly important for seismic hazard and engineering seismology. There is considerable literature on empirical attenuation curves that summarize the reduction of observed seismic motion with distance from faults (e.g., Abrahamson et al., 2014; Atkinson & Boore, 1995; Boore et al., 2013). Computer simulations of ground motion augment the empirical attenuation curves with additional data points associated with (rarely observed) moderate and large events and very short propagation distances (Graves et al., 2011; Liu et al., 2006; e.g. Pitarka et al., 2000). A second key goal of this work is to clarify aspects of fault motion responsible for the general structure of typical ground motion attenuation curves.

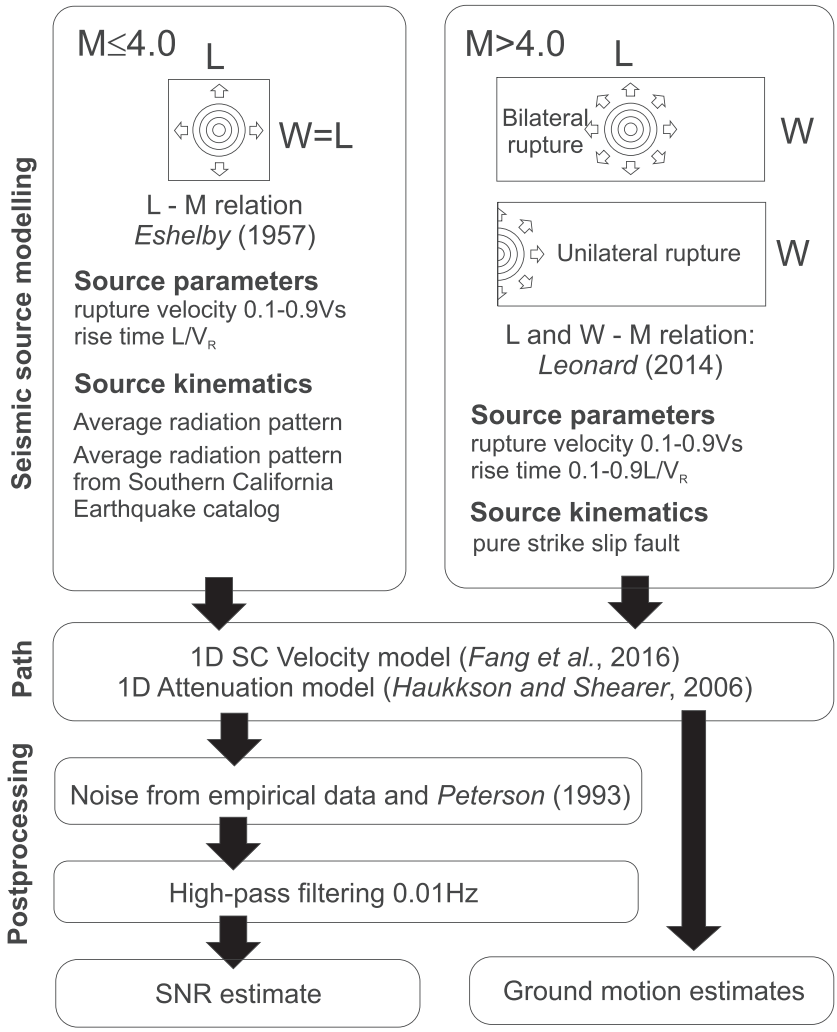

Figure 1. A schematic flow chart of modeling ruptures and calculating properties of ground motion.

In the following sections we investigate with calculations of seismic waveforms theoretical limits to detection of earthquakes with magnitudes in the range −1.0 to 6.0 and provide a basic understanding of expected ground motions of earthquakes at short epicentral distances. The calculations are based on forward modeling of seismic waveforms using the discrete wavenumber method (Bouchon, 1977, 1981, 2003) and seismic velocity and attenuation properties representative of the crust in Southern California (Fang et al., 2016; Hauksson & Shearer, 2006). The examined source characteristics include varying magnitudes, different stress drops, slow and fast rupture velocities, varying rise times, and different focal mechanisms. In section 2, we describe the methods used to calculate synthetic waveforms to assess detectability of small earthquakes and analyze near-fault ground motions of larger earthquakes. The results on these topics, presented in section 3, highlight the importance of rupture speed and rise time (in addition to magnitude) on detectability and ground motions of seismic events. The radiation pattern is shown to have a dominant effect on the shape of attenuation curves at short distances. The results are summarized and discussed in the final section 4.

2. Methodology

2.1. Source Modeling

We extend the original modeling scheme of Kwiatek and Ben-Zion (2016) to account for more realistic source processes and wave propagation effects. The employed modeling scheme is presented in Figure 1.

For events with $-1.0 \le M \le 4.0$ the seismic source is modeled assuming a rectangular fault with an area $A = WL$ with W and L being the fault width and length, respectively. The rupture starts at the center of fault, propagates radially with constant velocity V_R, and stops at the fault edges. The rupture process is described by three key parameters: average slip over the fault surface $\overline{u}$, rupture velocity V_R, and rise time τ. For convenience, the average slip and rise time are parameterized using seismic moment and static stress drop. The average slip over the fault is calculated from the seismic moment using: $\overline{u} = M_0(GWL)^{-1}$, where $G = \rho V_S^2$ is the shear modulus with ρ and V_S being mass density and shear waves velocity, respectively, and G = 34 GPa for the assumed hypocentral depths (see next section). The seismic moment $M_0 = GP_0$, where P_0 is the potency, is linked with magnitude using the quadratic potency-magnitude scaling relation of Ben-Zion and Zhu (2002): $\log_{10}P_0 = d + cM + \gamma M^2$. The parameters d and c are as in Table 2 of Ben-Zion and Zhu (2002) and γ is adjusted within the data uncertainties to the value $\gamma = 0.0712$ to fit the moment of M 6 event based on the moment-magnitude relation of Hanks and Kanamori (1979). The relation between seismic moment M_0 and fault area WL is established through static stress drop $\Delta\sigma$ using circular crack-like source of Eshelby (1957): $\Delta\sigma = (7/16)M_0 r^{-3}$, which is typically used for small events. To convert circular to rectangular fault area, we assume that $L = W$ and use $\pi r^2 = LW$. Finally, the rise time τ is fixed to be the rupture duration T; that is, $\tau = T = L/V_R = W/V_R$. The assumed rise time is not significantly different from that calculated using various analytical and empirical models (e.g., Boatwright, 1980; Sato & Hirasawa, 1973; Shaw, 2013). This parameterization is used to quantify the detection limits of small earthquakes and to assess features of ground motions at small epicentral distances.

To model events with $M > 4.0$, we use scaling relations developed for intraplate strike slip earthquakes (Leonard, 2014, Table 4), which directly relate magnitude with average slip $\overline{u}$, fault length L, and width W as follows: $\overline{u} = 10^{(M-6.85)/2}$, $W = 10^{(M\,-\,3.88)/2.5}$, and $L = 10^{(M\,-\,4.17)/1.677}$. However, the rise time τ has significant impact on the amplitude of the radiated waves. For crack-like ruptures, τ is the same as the rupture duration T or somewhat larger (especially near the hypocenter) since the slip cessation is associated with arrest waves that propagate back from the rupture boundaries (e.g., Ben-Zion et al., 2012). For pulse-like rupture, the slip duration and τ at each point can be significantly shorter than the rupture duration (e.g., Haskell, 1964; Heaton, 1990) due to various dynamic and geometrical mechanisms that arrest the slip while the rupture is propagating (e.g., Ben-Zion, 2001; Zheng & Rice, 1998). To account for a reasonable range of possibilities, the rise time in the simulations of $M > 4.0$ events is parameterized as

$$\tau = cT = cL/V_R, \tag{1}$$

where c is a numerical factor varying from 0.1 to 1. The elementary slip rate function is a smooth ramp with a spectral shape parameterized by the rise time τ as

$$\dot{u}(\omega) = -i\pi\frac{\tau}{2}(z - 1/z)^{-1}, \tag{2}$$

with $z = \exp(\omega\pi\tau/4)$. Examples of the source time functions for fast-propagating crack- and pulse- like M 6 earthquakes are presented in the supporting information, Figure S1.

The selected parameterization of source time function convolved with the rupture front propagation history produce a variety of far-field displacement spectra (Figure S2 in the supporting information). At sufficiently large epicentral distances, the decay of the displacement spectra at high frequencies is dominated by a slope following f^{-2}. For shorter distances, an interplay between f^{-1} and f^{-2} spectral decay slopes is clearly visible in agreement with theoretical expectations for Haskell-type sources (Haskell, 1964). A higher decay slope of f^{-3} is also visible for the displacement spectra of crack-type sources at high frequencies, as a consequence of the smooth shape of the elementary source time function. These seismic source features are expected to influence the amplitudes and distribution of ground motions in the performed simulations.

The assumed source model for $M > 4$ events is used to study details of ground motion at short epicentral distances from M 6.0 right-lateral strike-slip earthquake with hypocenter at a depth of 8.5 km. The selected strike-slip kinematics is representative for recent moderate events in Southern California. There are eight events in the Southern California focal mechanism catalog with $M_W > 6.0$ during 1987–2010 (Yang et al., 2012). Of these, seven have rake between $-180° <$ rake $< -159°$ or $159° <$ rake $< 180°$ (i.e., strike-slip kinematics), and the dip angle of five events is $\ge 85°$. Two rupture scenarios of moderate events are considered in the simulations. In the first scenario, the earthquake nucleates at the center of a

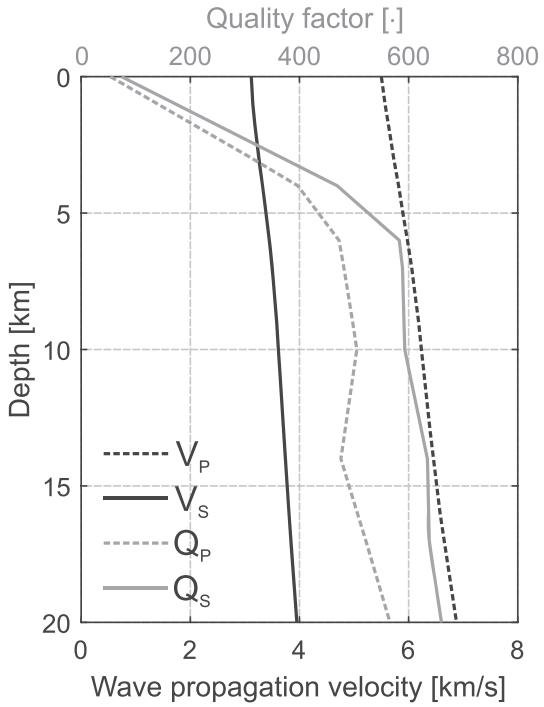

Figure 2. The 1-D structural model used in calculations of synthetic seismograms based on the *P* and *S* wave velocity results of Fang et al. (2016) and quality factors models of Hauksson and Shearer (2006).

vertical rectangular fault ($W = 7.0$ km and $L = 12.5$ km, cf. Figure 1) and propagates radially with constant rupture velocity until arrested at the fault edges. After reaching the top and bottom of the fault, the initially circular rupture front becomes a bilateral rupture. In the second scenario, the nucleation point is located at the same depth but at one edge of the fault (cf. Figure 1). In this case, a short initial circular propagation phase is followed by unilateral rupture propagation along the longer fault dimension *L*.

All modeled earthquakes are assumed to be pure double couples. Small non-double-couple components have been observed in Southern California and elsewhere (e.g., Ross et al., 2015; Stierle et al., 2014). However, the observed range of non-double-couple components does not have a significant effect on the resulting ground motions and signal-to-noise ratio (SNR) of *P* and *S* waves (Kwiatek & Ben-Zion, 2016).

2.2. Synthetic Seismograms

The synthetic seismograms are calculated using the discrete wavenumber technique (Bouchon, 1977, 1981, 2003) and the account for the free surface effect. The assumed crustal structure incorporates 1-D azimuthally averaged *P* and *S* wave velocities based on the 3-D tomography results of Fang et al. (2016), and the 1-D attenuation models of Hauksson and Shearer (2006) for southern California (Figure 2). The velocities change smoothly in the depth interval 0–20 km from 5.5 to 6.9 km/s for *P* waves and 3.1 to 4.0 km/s for *S* waves. For the sake of simplicity and generality, the assumed velocity model does not include near-surface velocity gradients related to sediments. Also, we do not consider sharp velocity discontinuity at shallow midcrustal depth (e.g., Dreger & Helmberger, 1991) that can influence ground motions characteristics. Existence of such layer complicates the wavefield, leading to multiple *S* reflections in the material above, modifies surface wave amplitudes, and changes the transmissivity of seismic energy from events located below the layer (Dreger & Helmberger, 1991; Catchings & Kohler, 1996). The quality factors of *P* and *S* waves (third model for Q_P and second model for Q_S from Hauksson and Shearer, 2006) increase rapidly in the first 4 km from about 100 to 400–500, and then continue to increase slowly reaching $Q_P = 575$ and $Q_S = 660$ at a depth of 20 km.

During the modeling of synthetic seismograms, the sampling rate is dynamically adjusted to obtain correct reproduction of waveform shapes and preserve the high-frequency content. This is especially important for the smallest events with high assumed rupture velocity and stress drop, where the expected frequency content is the highest, (cf. Kwiatek & Ben-Zion, 2016).

2.3. Signal-to-Noise Ratios

To calculate signal-to-noise ratio (SNR), we first create a time series generated from power spectral density of the average noise model designed in Kwiatek and Ben-Zion (2016). That model was developed using the average of low and high noise models of Peterson (1993) at low frequencies, extended to high frequencies using empirical data from natural and induced earthquakes.

Before calculating SNR, the synthetic noise trace and synthetic seismograms are filtered using a second-order 0.01 Hz high-pass Butterworth filter. This removes very low frequency oscillations of synthetic noise traces, but does not influence the $M < 4$ signals considered in this study. The standard deviation of the noise level is calculated from the filtered noise trace using

$$\sigma^{\text{noise}} = \text{std}\left\{\sqrt{N_x^2(t)+N_y^2(t)+N_z^2(t)}\right\}_{t\in T^{noise}}, \quad (3)$$

where $N_x(t)$, $N_y(t)$, and $N_z(t)$ are the three components of the ground velocity noise trace.

The signal level is measured separately for the *P* and *S* waves. A 1-D ray tracing is used to calculate the expected arrival times of the body waves in the synthetic seismograms. For *P* waves, a time window is

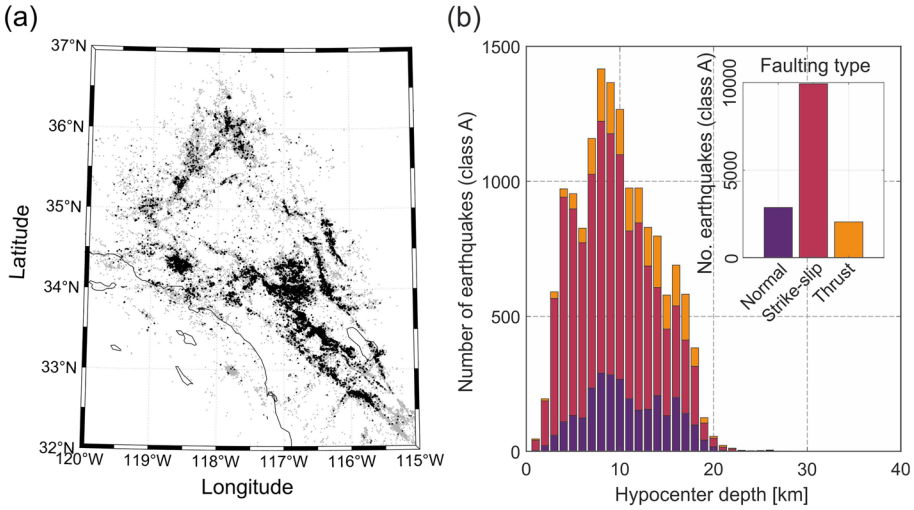

Figure 3. (a) Epicentral distribution of earthquakes (black and gray dots) in the Southern California catalog of Hauksson and Shearer (2006). The used 14,830 earthquakes with class-A quality focal mechanisms in the catalog of Yang et al. (2012) are shown with black dots. (b) Histogram of class-A quality events as a function of hypocentral depth with colors denoting focal mechanism type. The inset displays faulting type statistics of the used catalog.

selected around the first P arrival t^P using, $T^P = [t^P - 0.03s, t^P + 0.5(t^S - t^P)]$. The maximum amplitude of P wave is searched in the window T^P using all three components of the synthetic seismograms V_x,V_y, and V_z:

$$V^{\mathrm{P}}_{\mathrm{max}} = max\left\{\sqrt{v^2_{\mathrm{x}}(t)+v^2_{\mathrm{y}}(t)+v^2_{\mathrm{z}}(t)}\right\}_{t\in T^{\mathrm{P}}} \tag{4}$$

The corresponding SNR ratio is then calculated as

$$\mathrm{SNR}^{\mathrm{P}} = V^{\mathrm{P}}_{\mathrm{max}}/\sigma^{\mathrm{noise}} \tag{5}$$

A similar procedure is used to calculate the SNR for the S wave using a generalized time window $T^S = [t^S - 0.03s, t^S + 3(t^S - t^P)]$, adjusted to the expected S wave arrival and duration of the rupture process. As in Kwiatek and Ben-Zion (2016), an SNR of 20 dB means that the maximum velocity amplitude of P or S wave arrival is 10 times larger than the noise level. The detection limit of a single station is assumed to be 0 dB and may be decreased to −12 dB using an array of sensors (Inbal et al., 2015; Meng & Ben-Zion, 2018b).

2.4. Detection Limits

To analyze detection limits of small earthquakes, synthetic seismograms of events with magnitudes M between −1.0 and 4.0 are calculated for stations at epicentral distances ranging from 0.1 to 50 km assuming different source characteristics. To investigate the influence of source properties on the SNR, we consider a range of rupture velocities from 0.1 V_S to 0.9 V_S and three static stress drops equal to 0.1, 1.0, and 10 MPa. We assume constant hypocenter depth of 8.5 km, which corresponds to the peak in the hypocentral depth distribution of Southern California earthquakes (Figure 3).

To estimate detection limits for a particular combination of source characteristics, we average information from many synthetic seismograms and corresponding SNRs as follows. For selected combination of source parameters (magnitude, stress drop, rupture velocity), synthetic seismograms of event at a depth of 8.5 km are calculated 200 times for a considered range of epicentral distances. Each calculation uses a different focal mechanism and a random azimuth between the earthquake epicenter and seismic station. The focal mechanism for each synthetic seismogram realization is sampled using one of the following two strategies:

Strategy A: Focal mechanism parameters are randomly drawn from a subset of Southern California (SC) catalog of 14,830 fault plane solutions for years 1981–2014 with highest "class-A" quality (Yang et al., 2012). The observed SC catalog of fault plane solutions for these years is dominated by strike-slip mechanisms (Figure 3b).

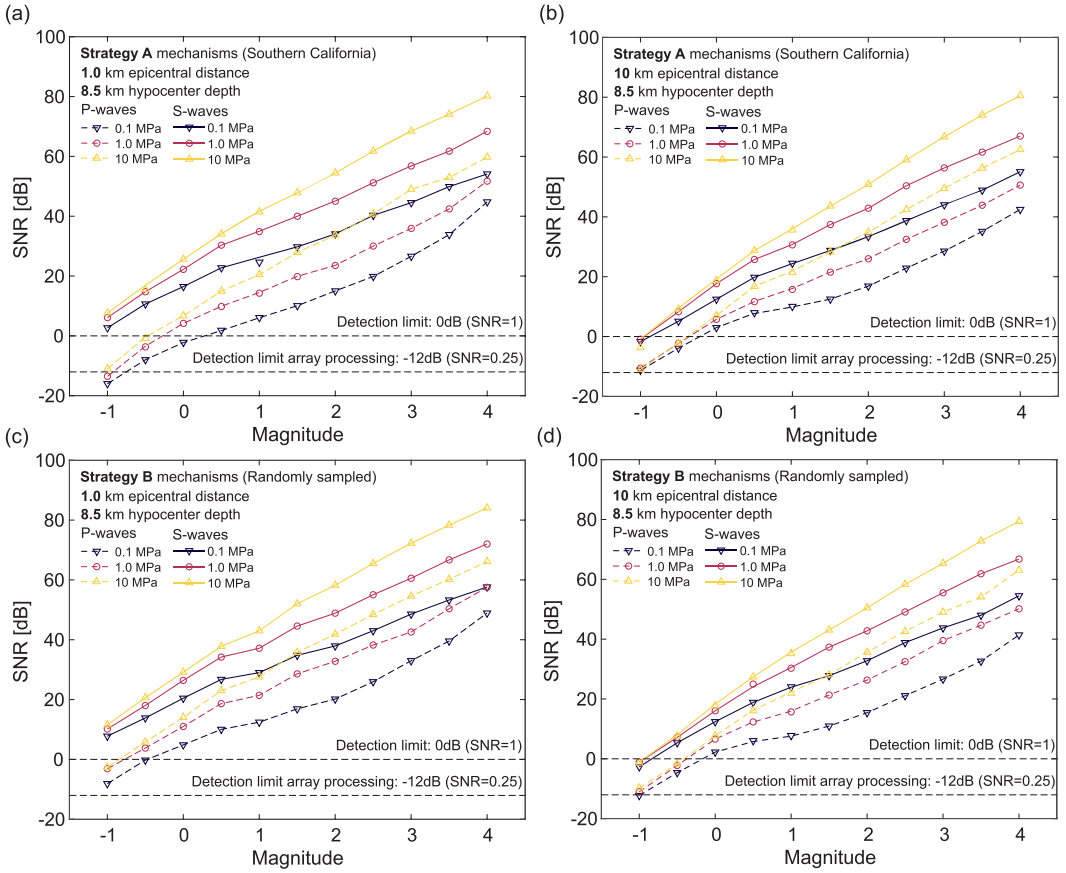

Figure 4. Maximum SNR of *P* and *S* waves (dashed and solid lines, respectively) as a function of magnitude for epicentral distances of 1 km (a, c) and 10 km (b, d). The curves are parameterized for stress drops of 0.1, 1.0, and 10 MPa (color scale). Figures 4a, 4c and 4b, 4d show SNRs averaged from focal mechanisms sampled using strategies A and B, respectively (see text for details).

Strategy B: Focal mechanism parameters are selected randomly following the procedure described in Boore (1986). This is equivalent to our earlier study (Kwiatek & Ben-Zion, 2016), which provided a generic assessment of ground motions and SNRs independent of source kinematics.

Having a set of 200 synthetic seismograms sampled with either strategy, the corresponding SNRs calculated using Equation 4 are averaged. This means that the calculated ground motions are independent of station azimuth and specific to the selected source characteristics and strategy of focal mechanism sampling.

2.5. Near-Fault Ground Motions

The results on this topic include simulations and analysis of near-fault ground motions of small and moderate events from M −1 to M 4, and a number of simulations for M 6 earthquakes associated with different rupture processes.

For events with M ranging from −1 to 4, the maximum recorded ground motions V_{max} is calculated from the synthetic seismograms and investigated as a function of epicentral distance, $V_{max}(R)$. The examined source parameters influencing $V_{max}(R)$ include earthquake magnitude, static stress drop, rupture velocity, and focal mechanism sampling strategy.

For the M 6 events, we examine features of ground motion distribution at the surface as a function of epicentral distance and azimuth from the direction of rupture propagation, $V_{max}(R, \Phi)$. We simulate different rupture scenarios by modifying the rupture velocity V_R (0.1–0.9V_S) and rise time τ (0.1–1.0 L/V_R). For a range of rupture velocities and rise times, we test two end-member cases associated with bilateral and unidirectional ruptures (cf. Figure 1).

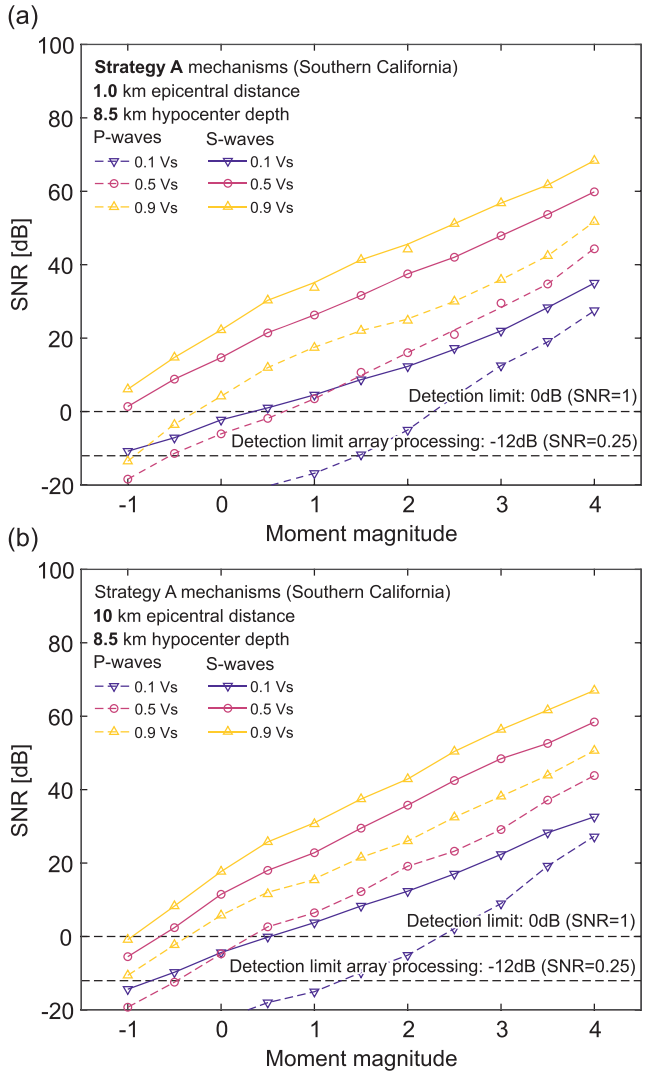

Figure 5. Maximum SNR of ground velocity amplitude as a function of magnitude for epicentral distances of 1 km (a) and 10 km (b) averaged over focal mechanisms drawn from SC catalog (strategy A). Yellow, red, and violet curves are parameterized by rupture velocities of $0.9V_S$, $0.5V_S$, and $0.1V_S$, respectively. The assumed static stress drop is 1 MPa.

3. Results

3.1. Detection Limits of Regular Earthquakes

Figures 4a and 4b presents SNRs of *P* and *S* waves for events with standard rupture velocity ($V_R = 0.9V_S$), associated with different magnitudes and focal mechanisms drawn from the Southern California earthquake catalog (strategy A). Corresponding generic cases using random focal mechanisms (strategy B) are shown in Figures 4c and 4d. All curves are calculated for stations located at 1 and 10 km epicentral distance from the sources at a depth of 8.5 km (8.6 and 13.1 km hypocentral distance, respectively), which is dominant depth of events in the SC earthquake catalog (Figure 3b). The calculated curves are parameterized by static stress drop values of 0.1, 1.0, and 10 MPa.

The observed SNRs decrease, as expected, with decreasing magnitude and static stress drop. Earthquakes with $M = -1.0$ are still detectable at 1 km epicentral distance using *S* waves, regardless of the static stress drop; however, the corresponding *P* wave amplitudes are already at the detection limits (Figures 4a and 4c). At 10 km epicentral distance, the conventional detection limit is $M = -0.7$ when *S* phase is considered (Figures 4b and 4d), although events with $M = -0.7$ and lower magnitudes may be detectable with array processing. The ratio between maximum velocity amplitudes of *P* and *S* waves V^{S}_{max} and V^{P}_{max} is approximately constant (=0.1, =20 dB) for the same magnitude and stress drop. As discussed in Kwiatek and Ben-Zion (2016), this corresponds to differences in *P* and *S* waves radiation related to the assumed shear source.

With increasing *M*, the variations of maximum velocity amplitudes (and therefore SNR) increase for events characterized by different static stress drops. For *M* 4.0, the difference in SNR may reach ~25 dB for events characterized by 0.1 and 10 MPa static stress drop at 10 km epicentral distance (e.g., Figure 4b). For the same epicentral distance and $M - 0.5$, the SNR is essentially the same regardless of the stress drop. The results presented in Figure 4 are comparable to those obtained using homogeneous velocity and attenuation structures (Kwiatek & Ben-Zion, 2016).

3.2. Detection Limits of Slow Earthquakes

Figure 5 summarizes the influence of rupture velocity of events with different magnitudes on the maximum amplitude of ground velocity of *P* and *S* waves at epicentral distances of 1 and 10 km. The events are assumed to have hypocenter depth of 8.5 km deep and static stress drop of 1 MPa, and the results are averaged over focal mechanisms sampled from the SC catalog (strategy A). The results show that lowering the rupture velocity leads to a rapid decrease in the observed ground motions of *P* and *S* waves, and thus the corresponding SNR. At 1 km epicentral distance and $V_R = 0.5V_S$, the detection limits using *S* and *P* waves are *M* −1.0 and 0.5, respectively. For a slow rupture velocity of $V_R = 0.1V_S$, the corresponding detection thresholds for *S* and *P* waves are *M* 0.5 and *M* 2.2, respectively.

3.3. Ground Motions of Regular Earthquakes at Short Distances

Figure 6 presents the dependence between maximum ground velocity amplitude of *S* wave V^{S}_{max} and epicentral distance ranging 0.1 to 5 km for earthquakes with static stress drops of 0.1, 1.0, and 10 MPa assuming standard rupture velocity of 0.9 V_S and constant hypocenter depth of 8.5 km. The curves are parameterized by magnitude and focal mechanism sampling strategy. The modeling results are compared with average peak ground velocities observed in different magnitude ranges for earthquakes recorded in the San Jacinto Fault Zone in California (cf. Figure 17 in Kurzon et al., 2014). The modeled results exhibit larger values of V^{s}_{max} for earthquakes having larger magnitudes and static stress drops. At distances exceeding 5 km, a progressive

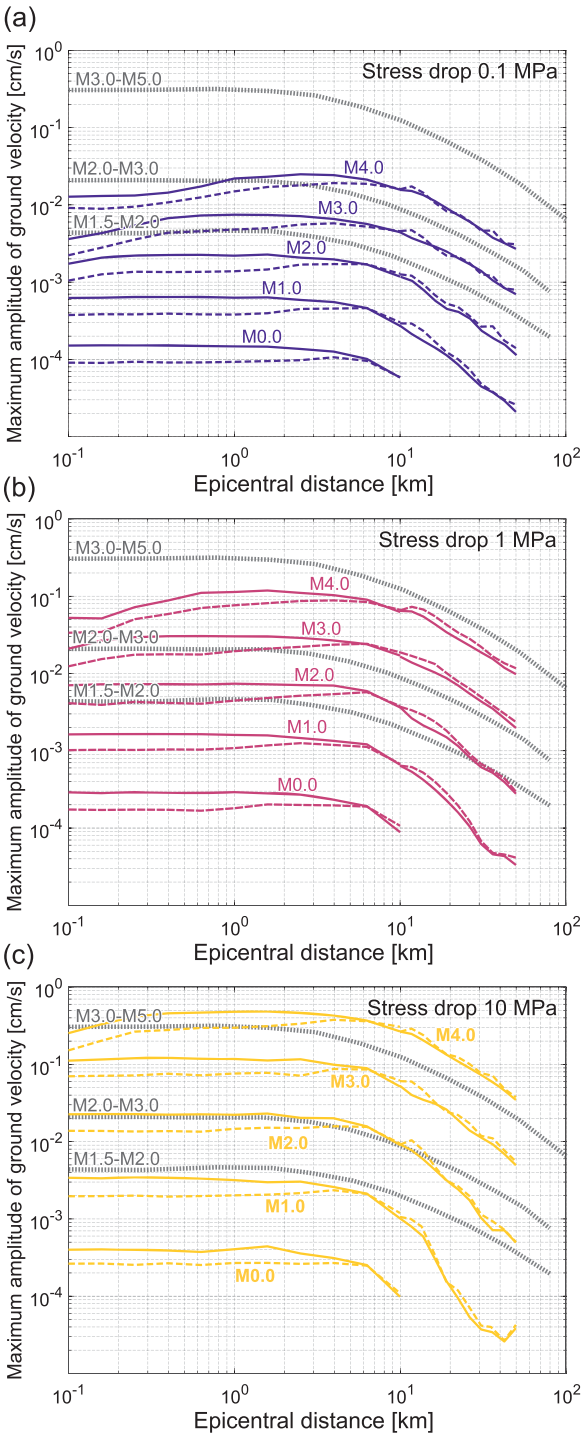

Figure 6. Dependence of maximum amplitude of S waves, V^{S}_{max} on epicentral distance for earthquakes with stress drops of to 0.1, 1.0, and 10 MPa (subfigures a–c). Each curve is parameterized by earthquake magnitude and sampling strategy of focal mechanisms. Solid and dashed curves represent V^{S}_{max} calculated from synthetic seismograms with focal mechanisms drawn randomly (strategy B) or sampled from the SC focal mechanism catalog (strategy A), respectively. Gray dotted lines represent V^{S}_{max} averaged in different magnitude ranges from earthquake data recorded in the San Jacinto Fault zone (cf. Figure 17, Kurzon et al., 2014).

drop-off in V^{s}_{max} is observed, with a slope of the drop-off in V^{s}_{max} at larger distances that is generally consistent with the observations of Kurzon et al. (2014). We also note that for the modeled small earthquakes with high stress drops, the values of V^{s}_{max} decrease more rapidly with increasing epicentral distance. This can be related to attenuation, which reduces the high-frequency content of the modeled waveforms, and is visible most clearly for events with high dominant frequencies, that is, those with small magnitudes and high stress drops. A more extended presentation of this issues is given by Kwiatek and Ben-Zion (2016).

At short epicentral distances, the simulated ground motions present an interesting nontrivial behavior. For small events with approximately $M < 2.0$, the modeled curves show generally a flattening at distances below 5 km. However, for larger events V^{s}_{max} seems to decrease at short epicentral distances without the plateau that characterizes small events. This effect becomes more prominent with lower stress drops and larger magnitudes. The different sampling strategies of focal mechanisms have persistent effect on the modeled ground motions, regardless of the assumed magnitude and static stress drop of the source (cf. solid and dashed lines in Figure 6). The observed average V^{s}_{max} values are lower at short epicentral distances (<8 km) when focal mechanisms are drawn from the SC catalog. However, for larger epicentral distances, the modeled V^{s}_{max} are similar regardless of the strategy of focal mechanism sampling. We return to these features in the discussion section.

3.4. Ground Motions of Moderate Slow and Fast Earthquakes

Figure 7 presents the expected surface distribution of maximum ground velocity amplitude, $V_{max}(\Delta, \Phi)$, as a function of epicentral distance Δ from the hypocenter and azimuth Φ from the rupture propagation direction (which is always to the north). The subplots show modeling outcomes of $V_{max}(\Delta, \Phi)$ for bilateral and unilateral rupture propagation and two extreme rupture velocities: $V_R = 0.9V_S$ and $V_R = 0.1V_S$. In all cases presented in Figure 7 we assumed crack-type ruptures ($c = 1.0$ in Equation 1), that is, the rise time is equal to the duration of the rupture process.

Regardless of the rupture propagation type and velocity, the observed $V_{max}(\Delta, \Phi)$ values are very low and do not exceed 1 cm/s in the areas of largest ground motions. The low ground motions are related to the assumed crack-type source time function with long gradual rise times of slip. The $V_{max}(\Delta, \Phi)$ decreases considerably with reduced rupture velocity, which further elongates the total duration of the source time function. The ground motions for slow rupture propagation of $0.1V_S$ are nearly 10 times lower than that for the fast rupture propagation. Finally, in these results, the spatial distribution of ground motions seems to be dominated by radiation pattern from the strike-slip event with relatively minor effects from the rupture directivity.

Figure 8 shows corresponding results of surface distribution of ground motions for pulse-like ruptures, where the rise time is equal only to 10% of the rupture duration ($c = 0.1$, cf. Equation 1). In this set of modeling results, the directivity effects dominate the ground motion distribution for fast rupture propagation (Figures 8a and 8b), leading to strong PGV values along the direction(s) of rupture propagation. The ground motions reach over 25 cm/s for a fast bilateral rupture propagation, whereas the

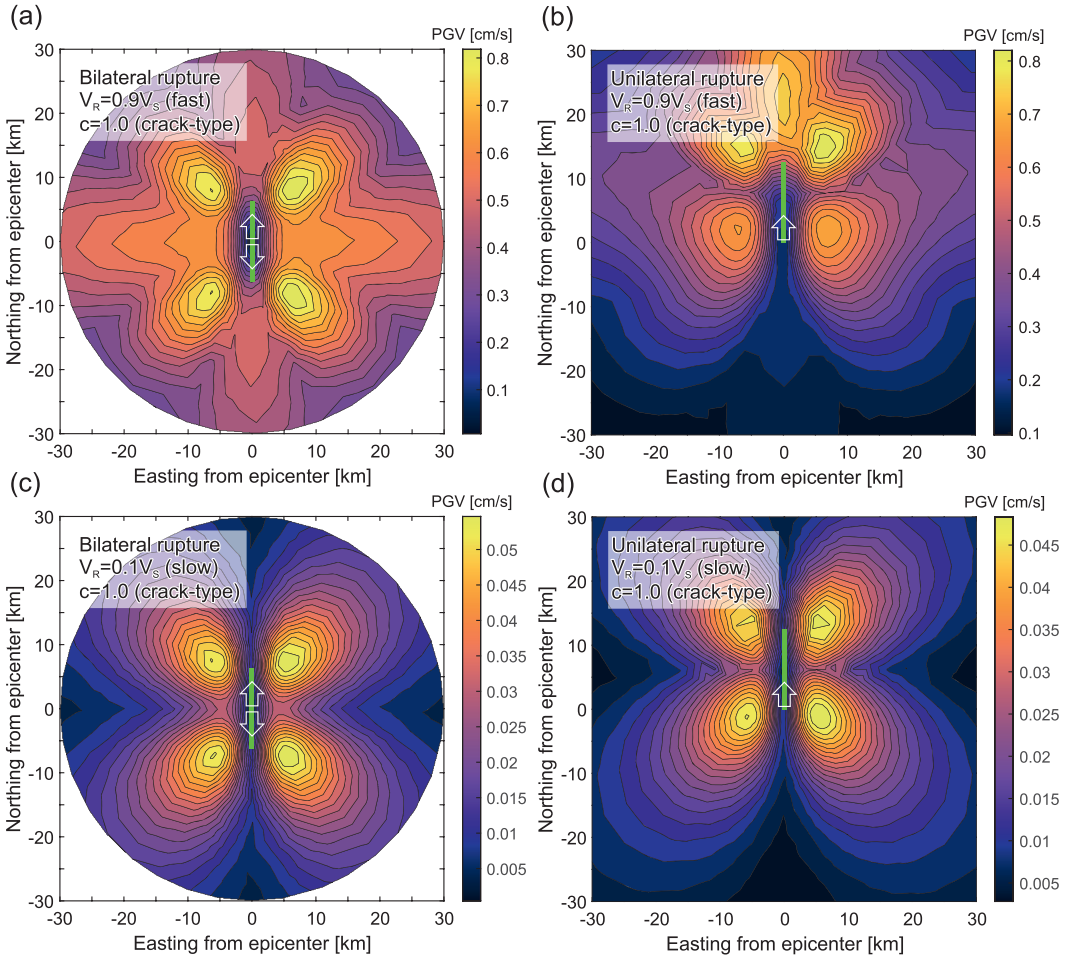

Figure 7. Distribution of maximum ground velocity amplitude at the surface expected from a strike-slip slip crack-type (c = 1.0) M 6.0 earthquake (strike/dip/rake = 0°/90°/0°, nucleation point depth = 8.5 km L = 12.5 km W = 7.0 km) as a function of epicentral distance from the nucleation point and azimuth from the rupture propagation direction. The surface fault trace is shown with green color, and the rupture propagation direction is marked with arrow(s). Subfigures show ground motions for (a, c) bilateral and (b, d) unilateral rupture propagation and (a, b) fast and (c, d) slow rupture velocities.

corresponding unilateral propagation produces the largest simulated PGV of ~37 cm/s. For slow ruptures propagation of 0.1V_S, the surface distributions of ground motions generated by crack-type (Figures 7c and 7d) and pulse-type (Figures 8c and 8d) ruptures are comparable. However, the maximum amplitude of ground motions for pulse-type rupture is 3–4 times higher than that of crack-type events.

4. Discussion

Understanding the factors influencing seismic ground motion is important for earthquake physics, detection of regular and slow events, as well as seismic hazard assessments especially at short epicentral distances where the available data are scarce. To provide information for these topics, we simulate ground motions from finite-size earthquakes with magnitudes ranging from M −1.0 to 6.0, different stress drops, directivity effects, rupture velocities, and rise times. The modeling is done assuming crustal structure and earthquake properties observed in Southern California, but various features are general and apply (perhaps with modified amplitudes) to other regions.

Constraining focal mechanisms to a particular subset has a clear effect on ground motions at short epicentral distance (Figure 6). We observe that strike-slip dominated mechanisms reduce the ground motions close to faults in comparison to a generic case of randomly selected mechanisms. To clarify this further, we follow the procedure of Boore and Boatwright (1984) to estimate average radiation pattern correction

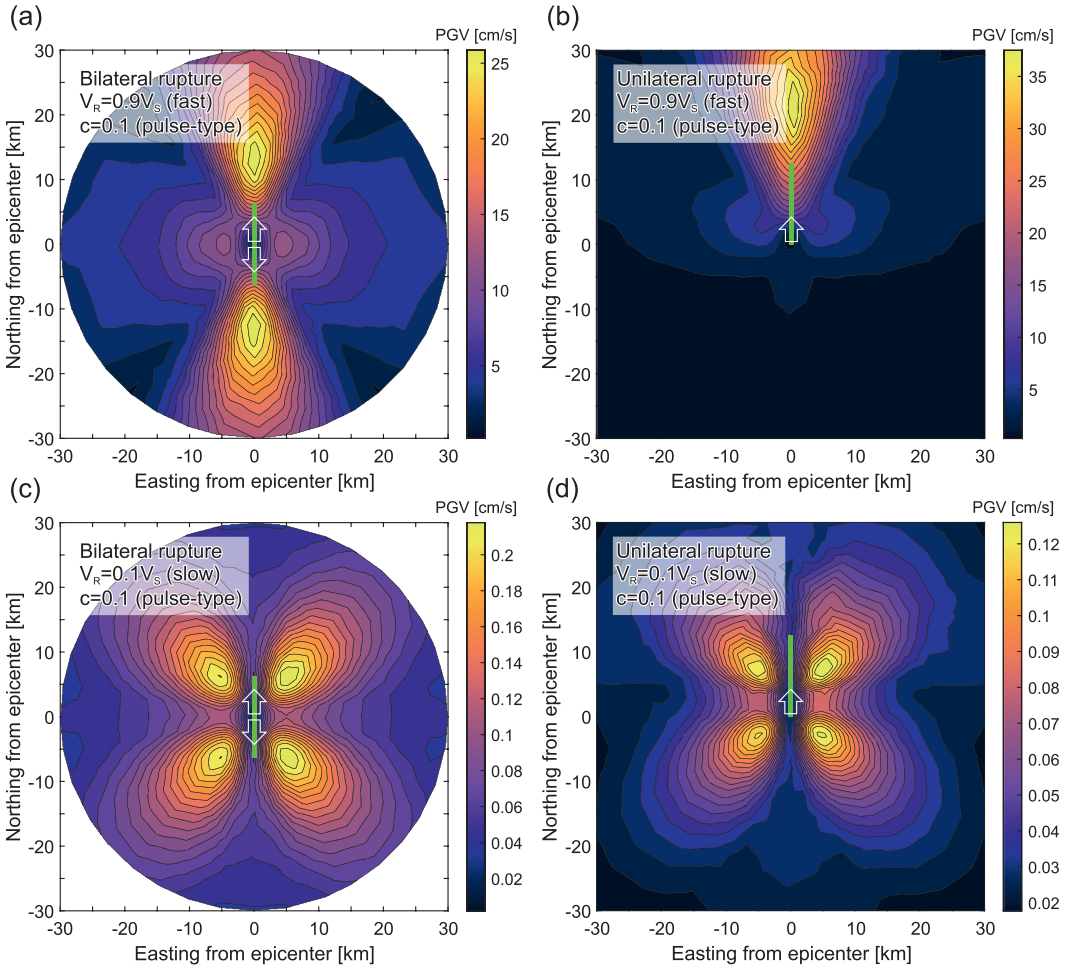

Figure 8. Distribution of maximum ground velocity amplitude at the surface expected from a strike-slip slip pulse-type ($c = 0.1$) M 6.0 earthquake. Subfigures shows ground motions for (a, c) bilateral and (b, d) unilateral rupture propagation and (a, b) fast and (c, d) slow rupture velocities.

coefficients. We first model takeoff angles at epicentral distances ranging from 0.1 to 100 km from an event located at 8.5 km depth. Then, we calculate the expected radiation of *P* and *S* waves using double-couple radiation pattern (Aki & Richards, 2009; Boore & Boatwright, 1984; Kwiatek & Ben-Zion, 2016; Ou, 2008) and random station azimuth. The strike, dip, and rake are either chosen randomly or randomly from the SC focal mechanism catalog. The procedure is repeated 60,000 times and the resulting ensembles of *P* and *S* wave radiation coefficients sampled with strategies A and B are averaged (Boore & Boatwright, 1984) for each epicentral distance.

Figure 9a presents changes in the average *P* and *S* wave radiation coefficients expected from random and SC-based focal mechanisms as a function of epicentral distance. Random sampling of focal mechanisms produces average *P* and *S* wave radiation coefficients close to 0.52 and 0.63, respectively (Boore & Boatwright, 1984). However, selection of focal mechanisms based the SC catalog leads to radiation coefficients that change with epicentral distances (black lines in Figure 9a). At shorter distances, the expected radiation of *P* and *S* wave is 1.2–1.4 times lower than the expectations using random focal mechanisms (Figure 9b). Close to 10 km epicentral distance, the radiation of *P* and *S* waves become comparable regardless of strategy of focal mechanisms sampling. This explains the persistent discrepancy of the simulated V^{S}_{max} in Figure 6 with the different strategies of focal mechanism sampling.

The saturation of ground motions at close epicentral distances (cf. Figure 6) is an important feature that is represented in Ground Motion Prediction Equations (GMPE) developed for different regions (see Atkinson et al., 2016, and references therein). Yenier and Atkinson (2015) used an equivalent point source model to

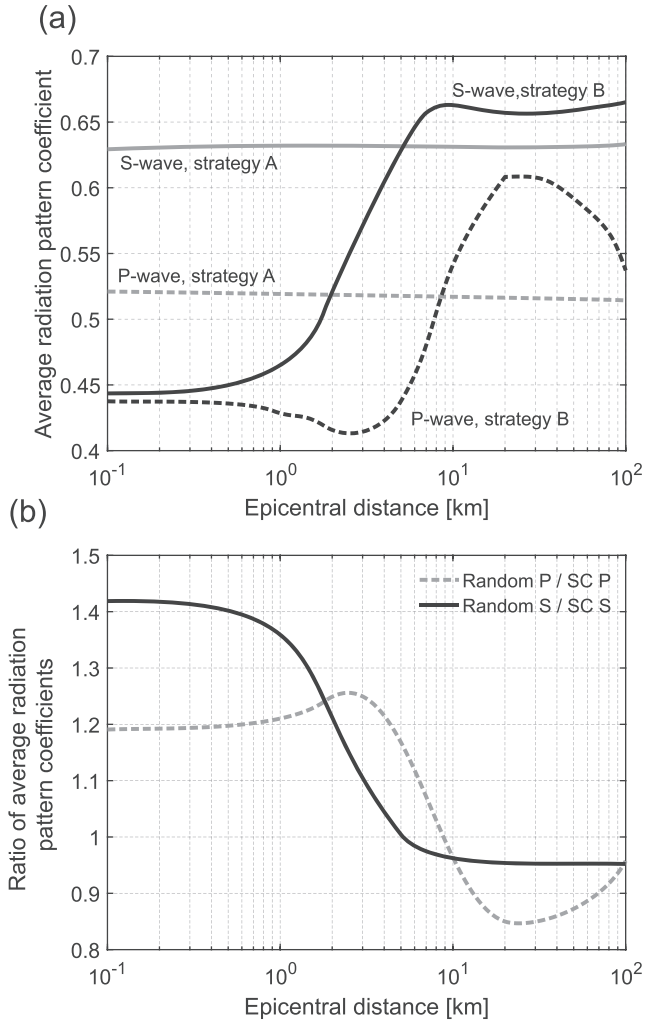

Figure 9. (a) Changes in average radiation pattern coefficients of *P* (dashed black line) and *S* waves (solid black line) with epicentral distance for focal mechanisms randomly drawn from the SC catalog. Gray lines show corresponding generic average radiation pattern coefficients for randomly sampled focal mechanisms (0.52 and 0.63 for *P*, and *S* waves, respectively; cf. Boore & Boatwright, 1984 for details). (b) The quotients between average radiation pattern coefficient calculated using mechanisms drawn randomly and sampled from SC focal mechanism catalog for *P* (dashed line) and *S* waves (solid line) (cf. Figure 6).

develop generic GMPE, where the observed near-distance saturation in ground motions is modeled assuming a site-dependent *effective distance* parameter, $R = \sqrt{D^2 + h^2}$, where D is hypocentral distance and the additional term h called the *effective* or *pseudo depth*. This site-dependent parameter scales predominantly with earthquake magnitude. Increasing magnitude enhances the *effective depth* parameter, and therefore enlarges the saturation of the constant ground motions at short epicentral distances. However, as pointed out by Yenier and Atkinson (2015), this parameter likely aggregates influence from other source-related factors influencing the event size, such as static stress drop.

The larger the event dimension is (larger magnitude or lower stress drop), the more prominent is the depletion in ground motions in Figure 6 at short epicentral distances, even for the buried ruptures considered in our simulations with 8.5 km hypocenter depth. The depletion is clearly visible for events with magnitudes as low as $M = 3.0$ and is produced primarily by geometrical factors associated with the radiation pattern (cf. Figure 9) and rupture dimensions. Reduced stress drops lead to enhanced depletion of the ground velocity amplitude at short epicentral distances due to the relatively larger fault size for the same magnitude range (cf. Figures 6a and 6c). Lowering the static stress drop for a given magnitude corresponds to an increase of the *effective depth* parameter of Yenier and Atkinson (2015).

The simulations of ground motions of small events with $M \leq 4$ are done using the standard assumption that small events follow statistically a crack type behavior (e.g., Eshelby, 1957; Sato & Hirasawa, 1973). The geometrical and dynamic mechanisms leading to pulse-type events are stronger for larger events (e.g., Ben-Zion, 2001; Day, 1982; Lyakhovsky et al., 2016). However, there is evidence that small earthquake may also behave in pulse-like manner (e.g., Dreger et al., 2007; Mori & Hartzell, 1990; Uchide & Ide, 2010). The assumption of pulse-type behavior also for small event would lead generally to increased amplitudes of ground motions, similar to the results obtained from modeling pulse-type *M* 6.0 earthquakes.

Figure 10 presents the maximum simulated ground velocities averaged over different ranges of azimuths as a function of epicentral distance for events with different rupture velocities, rise times, and rupture directivities. The rupture velocity and rise time (crack- vs. pulse-type rupture) affect considerably the amplitude of the ground motion, but they do not influence the shape of the relative depletion of ground motion at short epicentral distances. However, the depletion of ground motion at very short distances is less pronounced for unilateral ruptures, which focus more energy near the fault, but for a given rupture directivity all curves diminish at the same rate with epicentral distance. We conclude that the shape of depletion of ground motions with distance and azimuth is governed by the earthquake size, focal mechanism, and source directivity. On the other hand, the amplitude of generated ground motion is governed, in addition to earthquake magnitude and stress drop, by rupture propagation velocity and the slip rise time or crack versus pulse rupture type. Interestingly, the modeled depletion in V^{S}_{max} is seemingly not reproduced for the largest earthquakes in Figure 17 of Kurzon et al. (2014), where the observed PGV values tend to flatten at short epicentral distances. This may be produced by the heterogeneous mixture of focal mechanisms in that study area along the San Jacinto fault zone (e.g., Bailey et al., 2010) and perhaps also dominant unilateral ruptures.

For the modeled *M* 6 event, the effects of source kinematics of the right-lateral strike-slip rupture are visible for slow propagation cases ($V_R = 0.1V_S$) (cf. Figures 7c and 7d and Figures 8c and 8d). The assumed

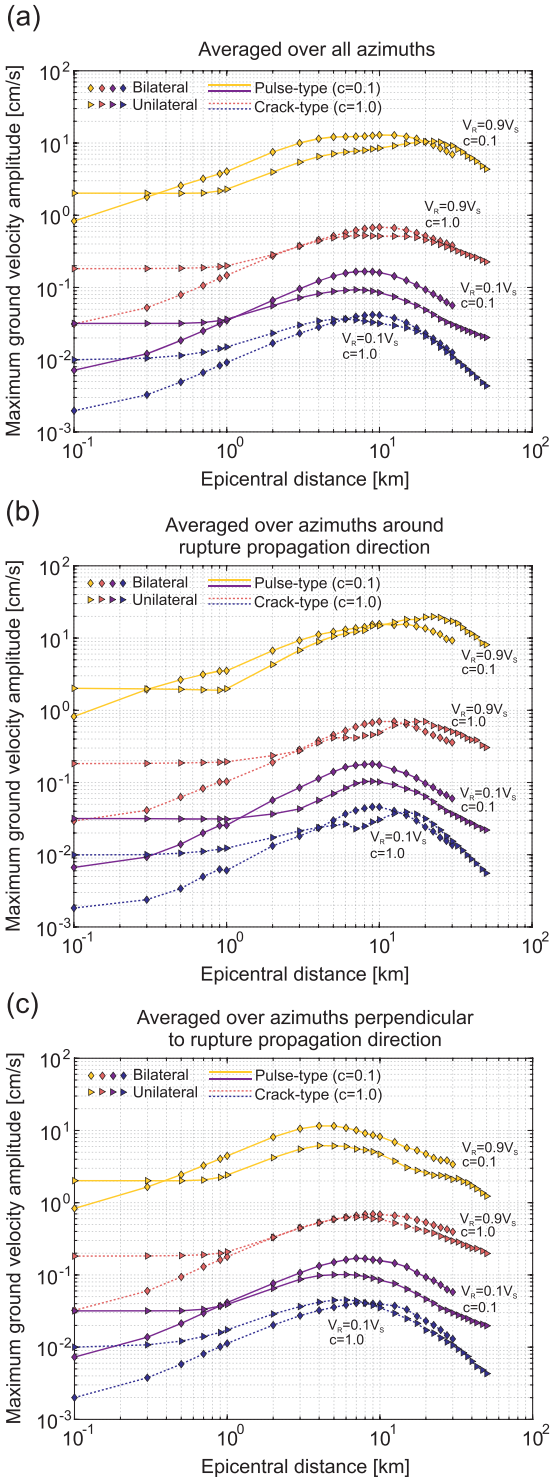

Figure 10. Maximum amplitude of ground velocity motions V^{S}_{max} versus epicentral distance averaged over (a) all azimuths, (b) azimuths around rupture propagation direction 315–45°, (c) azimuths perpendicular to rupture propagation direction (45–135°). Results for unilateral and bilateral ruptures are denoted by triangle and rhombus symbols, respectively, and calculations for short and long rise times (pulse- and crack-type ruptures) are shown with solid and dashed lines, respectively. Warmer colors reflect higher rupture velocities.

pure strike-slip focal mechanism produces little radiation of *P* and *S* waves close to the epicentral area, and most of seismic energy is radiated laterally and expresses on the surface at larger distances (typically >10 km). For the case of crack-type slow rupture (Figures 7c and 7d), the surface distribution of ground motions is dominated by the radiation pattern and directivity effects are not visible. Consequently, the resulting ground motions are very low (cf. Figure 10). However, fast crack-type earthquakes ($c = 1.0$, $V_R = 0.9V_S$, Figures 7a and 7b) produce signatures of rupture directivity. This is evidenced as an additional zone (unilateral) or zones (bilateral) with larger ground motions, located along the direction of rupture propagation. Also, the overall level of ground motions is ~10 times larger than that produced by slow crack-type ruptures (Figure 10). Fast pulse-like earthquakes with clear signatures of directivity produce extreme ground motions (Figures 8a and 8b) along the rupture propagation direction. The maximum ground motion is over 35 cm/s for the modeled fast pulse-like unilateral rupture, and over 25 cm/s for the bilateral fast pulse-like rupture. These values are 100–300 time higher than that modeled for the slow pulse-like earthquake (cf. Figure 10).

The results have implications for the design of seismic monitoring networks aiming to optimize the detection of slow earthquakes. It is intuitively expected that the strongest ground motions for fast-propagating strike-slip (especially pulse-like) earthquakes align along the rupture direction (=fault trace) (cf. Figures 8a and 8b). However, for slow-propagating (especially crack-like) ruptures, the maximum ground motions are located ±45° and away from the fault trace (e.g., Figures 7c and 7d), reflecting the dominance of earthquake kinematics and not the directivity effects.

As shown in Figure 10, changes of rupture velocity and rise time (crack vs. pulse rupture type) produce substantial changes to the maximum peak ground velocity and have significant consequences for near-fault seismic hazard and earthquake detectability. Moreover, the performance of the recording sensors (e.g., transfer function) and properties of acquisition systems (e.g., sampling rate) can further limit the detectability of earthquakes. To simulate approximately the transfer function effect of typical broadband seismometer for the largest synthetic events considered in this study, we filter the modeled waveforms of the *M* 6 event using a 0.01 Hz high-pass Butterworth filter. The consequence of this slight modification was a further reduction of the modeled ground motions (see Figures S3 and S4 in the supporting information). Although the surface patterns of ground motions of the slow, crack-type bilateral and unilateral earthquake were preserved, the observed amplitudes were reduced by a factor of 2 to a maximum value of 0.025 cm/s (Figure S3). These amplitudes of ground motions are observed ~10 km away from earthquakes epicenter, ±45° from the fault trace (Figures S3c and S3d, cf. with generic unfiltered case in Figures 7c and 7d). Such level of ground motions is still above the noise level observed in the frequency band of the broadband sensor (cf. Figure 8 in Kwiatek and Ben-Zion, 2016), so such an event is detectable by broadband instruments positioned at the right location. Nevertheless, the resulting ground motions are of intensity around I (~0.01 cm/s, following the Mercalli Scale). The low amplitude and frequency content makes such events generally not perceptible by humans (Du et al., 2017). This is in striking contrast with fast, pulse-like ruptures that produce V^{S}_{max} over

30 cm/s along the fault direction at the same distances of 10 km, which leads to VII intensity scale earthquake associated with "severe shaking" characteristics.

The sampling rate of the acquisition system can have significant effects on earthquake detectability. In our synthetic simulations this issue was suppressed using a sampling rate that is dynamically adjusted to preserve the high-frequency content of the waves. However, a reduction in the SNR is expected when the frequency content of the waves does not match the recording frequency band, which depends on the sampling rate at the upper limit of frequencies. To simulate this effect, we downsampled our original synthetic waveform data of $M \leq 4$ events to 200 and 100 Hz (the approximate lower-frequency limit of modern short-period sensors targeting detection of small events) and recalculated SNRs. The reduction in sampling rate was found to affect visibly, by up to 10 dB, only the SNR for the smallest modeled events ($M \leq 0$, higher stress drops 1–10 MPa) and at close distances (Figure S5). Low stress drop and large-magnitude events at short distances remained unaffected by the sampling rate decrease, and the potential effect of low sampling rate on SNR decreases with increasing distance. We conclude that the upper-frequency band of the acquisition system must be taken into account while optimizing the detection capabilities of small, high-frequency (high stress drop) events at short source-receiver distances (see additional discussion on this in Kwiatek & Ben-Zion, 2016).

5. Summary and Conclusions

Using the discrete wavenumber method to simulate seismograms of earthquakes with magnitudes ranging from −1.0 to 6.0, we investigate the influence of various seismic source characteristics on detection limits and ground motion distributions at short epicentral distances. For event detection, we examine the influence of magnitude, stress drop, and rupture velocity on SNR of events at distances not exceeding 50 km. For improved understanding of ground shaking at short epicentral distances, we examine in addition results for a representative M 6 strike-slip earthquake parameterized by different rupture velocity (0.1–0.9V_S), directivity effects (unilateral-bilateral), and propagation type (crack-type, pulse-like).

In addition to earthquake magnitude and path effects, the simulations highlight the importance of static stress drop and rupture velocity for detectability of small crack-type earthquakes with rise time comparable to rupture duration. Slow rupture propagation speed and lower stress drops reduce overall the seismic radiation and increase the magnitude detection limits of events. The saturation or even depletion of seismic ground motion at short epicentral distances can be understood primarily by geometrical properties associated with the earthquake size (magnitude, stress drop), radiation pattern, and hypocenter depth.

For larger earthquakes, effects associated with rupture propagation become more important for ground motions at short epicentral distances. Rupture directivity affects the shape of ground motion curves, while rupture velocity and rise time (and thus rupture type) influence only the overall amplitudes of the generated motions. The surface ground motion distribution of slowly propagating slip events is dominated by the focal mechanism (radiation pattern) and involves generally relatively low level of motion. In contrast, the ground motion distribution of fast earthquakes is affected significantly by rupture directivity and has large motions in the direction(s) of rupture propagation. The rise time and, hence, rupture type (crack vs. pulse type) has a profound effect on the level of ground motions. The clearly different amplitudes of ground motions generated by the considered events, and their spatial distributions, have important implications for near-fault seismic hazard and optimization of seismic network for detection of different types of events.

Data Availability Statement

The ground motion data simulated for various rupture scenarios presented in Figures 7 and 8 and S3 and S4 are available as data publication through GFZ data services website (Kwiatek & Ben-Zion, 2020), see this website (https://doi.org/10.5880/GFZ.4.2.2020.003).

Acknowledgments

We thank Michel Bouchon for the DWM code used to simulate ruptures in this study. G. K. thanks František Gallovič for valuable comments and acknowledges support from the Deutsche Forschungsgemeinschaft (DFG), Grant KW 84/4-1. Y. B. Z. acknowledges support from the U.S. Department of Energy (Award DE-SC0016520). The paper benefited from useful comments by Doug Dreger, Nori Nakata, and an anonymous referee.

References

Abrahamson, N. A., Silva, W. J., & Kamai, R. (2014). Summary of the ASK14 ground motion relation for active crustal regions. *Earthquake Spectra*, *30*(3), 1025–1055. https://doi.org/10.1193/070913EQS198M

Aki, K., & Richards, P. G. (2009). *Quantitative seismology*. Sausalito: University Science Books.

Atkinson, G. M., & Boore, D. M. (1995). Ground-motion relations for eastern North America. *Bulletin of the Seismological Society of America*, *85*(1), 17–30.

Atkinson, G. M., Emrah, Y., Sharma, N., & Convertito, V. (2016). Constraints on the near-distance saturation of ground-motion amplitudes for small-to-moderate induced earthquakes. *Bulletin of the Seismological Society of America*, *106*(5), 2104–2111. https://doi.org/10.1785/0120160075

Bailey, I. W., Ben-Zion, Y., Becker, T. W., & Holschneider, M. (2010). Quantifying focal mechanism heterogeneity for fault zones in central and southern California. *Geophysical Journal International*, *183*(1), 433–450. https://doi.org/10.1111/j.1365-246X.2010.04745.x

Ben-Zion, Y. (2001). Dynamic ruptures in recent models of earthquake faults. *Journal of the Mechanics and Physics of Solids*, *49*(9), 2209–2244. https://doi.org/10.1016/S0022-5096(01)00036-9

Ben-Zion, Y., Rockwell, T. K., Shi, Z., & Xu, S. (2012). Reversed-polarity secondary deformation structures near fault stepovers. *Journal of Applied Mechanics*, *79*(3). https://doi.org/10.1115/1.4006154. [online] Available from, https://doi.org/10.1115/1.4006154

Ben-Zion, Y., & Zhu, L. (2002). Potency-magnitude scaling relations for southern California earthquakes with $1.0 < M_L < 7.0$. *Geophysical Journal International*, *148*(3), F1–F5. https://doi.org/10.1046/j.1365-246X.2002.01637.x

Bergen, K. J., Johnson, P. A., de Hoop, M. V., & Beroza, G. C. (2019). Machine learning for data-driven discovery in solid Earth geoscience. *Science*, *363*(6433), eaau0323. https://doi.org/10.1126/science.aau0323

Boatwright, J. (1980). A spectral theory for circular seismic sources: Simple estimates of source dimension, dynamic stress drop, and radiated seismic energy. *Bulletin of the Seismological Society of America*, *70*, 1–27.

Boore, D. M. (1986). The effect of finite bandwidth on seismic scaling relationships. In *Earthquake Source Mechanics*, (Vol. 37, pp. 275–283). Washington, DC. [online] Available from: AGU. https://doi.org/10.1029/GM037p0275

Boore, D. M., & Boatwright, J. (1984). Average body-wave correction coefficients. *Bulletin of the Seismological Society of America*, *74*, 1615–1621.

Boore, D. M., Stewart, J. P., Seyhan, E., & Atkinson, G. M. (2013). NGA-West2 equations for predicting PGA, PGV, and 5% damped PSA for shallow crustal earthquakes. *Earthquake Spectra*, *30*(3), 1057–1085. https://doi.org/10.1193/070113EQS184M

Bouchon, M. (1977). Discrete wave-number representation of seismic source wave fields. *Bulletin of the Seismological Society of America*, *67*(2), 259–277.

Bouchon, M. (1981). A simple method to calculate Green's functions for elastic layered media. *Bulletin of the Seismological Society of America*, *71*(4), 959–971.

Bouchon, M. (2003). A review of the discrete wavenumber method. *Pure and Applied Geophysics*, *160*(3), 445–465. https://doi.org/10.1007/PL00012545

Catchings, R. D., & Kohler, W. M. (1996). Reflected seismic waves and their effect on strong shaking during the 1989 Loma Prieta, California, earthquake. *Bulletin of the Seismological Society of America*, *86*(5), 1401–1416.

Day, S. M. (1982). Three-dimensional finite difference simulation of fault dynamics: Rectangular faults with fixed rupture velocity. *Bulletin of the Seismological Society of America*, *72*, 705–727.

Dragert, H., Wang, K., & Rogers, G. (2004). Geodetic and seismic signatures of episodic tremor and slip in the northern Cascadia subduction zone. *Earth, Planets and Space*, *56*(12), 1143–1150. https://doi.org/10.1186/BF03353333

Dreger, D., Nadeau, R. M., & Chung, A. (2007). Repeating earthquake finite source models: Strong asperities revealed on the San Andreas Fault. *Geophysical Research Letters*, *34*, L23302. https://doi.org/10.1029/2007GL031353

Dreger, D. S., & Helmberger, D. V. (1991). Complex faulting deduced from broadband modeling of the 28 February 1990 upland earthquake ($M_L = 5.2$). *Bulletin of the Seismological Society of America*, *81*(4), 1129–1144.

Du, W., Goh, K. S., & Pan, T.-C. (2017). Methodology for estimating human perception to tremors in high-rise buildings. *Journal of Seismology*, *21*(4), 667–682. https://doi.org/10.1007/s10950-016-9628-y

Eshelby, J. D. (1957). The determination of the elastic field of an ellipsoidal inclusion, and related problems. *Proceedings of the Royal Society of London. Series A. Mathematical and Physical Sciences*, *241*(1226), 376–396. https://doi.org/10.1098/rspa.1957.0133

Fang, H., Zhang, H., Yao, H., Allam, A., Zigone, D., Ben-Zion, Y., et al. (2016). A new algorithm for three-dimensional joint inversion of body wave and surface wave data and its application to the Southern California plate boundary region. *Journal of Geophysical Research: Solid Earth*, *121*, 3557–3569. https://doi.org/10.1002/2015JB012702

Graves, R., Jordan, T. H., Callaghan, S., Deelman, E., Field, E., Juve, G., et al. (2011). CyberShake: A physics-based seismic hazard model for Southern California. *Pure and Applied Geophysics*, *168*(3–4), 367–381. https://doi.org/10.1007/s00024-010-0161-6

Hanks, T. C., & Kanamori, H. (1979). A moment magnitude scale. *Journal of Geophysical Research*, *84*(B5), 2348–2350. https://doi.org/10.1029/JB084iB05p02348

Haskell, N. A. (1964). Total energy and energy density of elastic wave radiation from propagating faults. *Bulletin of the Seismological Society of America*, *54*, 1811–1841.

Hauksson, E., & Shearer, P. M. (2006). Attenuation models (QP and QS) in three dimensions of the Southern California crust: Inferred fluid saturation at seismogenic depths. *Journal of Geophysical Research*, *111*, B05302. https://doi.org/10.1029/2005JB003947

Heaton, T. H. (1990). Evidence for and implications of self-healing pulses of slip in earthquake rupture. *Physics of the Earth and Planetary Interiors*, *64*(1), 1–20. https://doi.org/10.1016/0031-9201(90)90002-F

Inbal, A., Clayton, R. W., & Ampuero, J.-P. (2015). Imaging widespread seismicity at midlower crustal depths beneath Long Beach, CA, with a dense seismic array: Evidence for a depth-dependent earthquake size distribution. *Geophysical Research Letters*, *42*, 6314–6323. https://doi.org/10.1002/2015GL064942

Inbal, A., Cristea-Platon, T., Ampuero, J., Hillers, G., Agnew, D., & Hough, S. E. (2018). Sources of long-range anthropogenic noise in Southern California and implications for tectonic tremor detection. *Bulletin of the Seismological Society of America*, *108*(6), 3511–3527. https://doi.org/10.1785/0120180130

Johnson, C. W., Meng, H., Vernon, F., & Ben-Zion, Y. (2019). Characteristics of ground motion generated by wind interaction with trees, structures, and other surface obstacles. *Journal of Geophysical Research: Solid Earth*, *124*, 8519–8539. https://doi.org/10.1029/2018JB017151. [online] Available from:

Kong, Q., Trugman, D. T., Ross, Z. E., Bianco, M. J., Meade, B. J., & Gerstoft, P. (2018). Machine learning in seismology: Turning data into insights. *Seismological Research Letters*, *90*(1), 3–14. https://doi.org/10.1785/0220180259

Kurzon, I., Vernon, F. L., Ben-Zion, Y., & Atkinson, G. (2014). Ground motion prediction equations in the San Jacinto Fault zone: Significant effects of rupture directivity and fault zone amplification. *Pure and Applied Geophysics*, *171*(11), 3045–3081. https://doi.org/10.1007/s00024-014-0855-2

Kwiatek, G., & Ben-Zion, Y. (2016). Theoretical limits on detection and analysis of small earthquakes. *Journal of Geophysical Research: Solid Earth*, *121*, 5898–5916. https://doi.org/10.1002/2016JB012908

Kwiatek, G., and Ben-Zion, Y. (2020). in Southern California. V. 1.0. GFZ Data Services, https://doi.org/10.5880/GFZ.4.2.2020.003

Leonard, M. (2014). Self-consistent earthquake fault-scaling relations: Update and extension to stable continental strike-slip faults. *Bulletin of the Seismological Society of America*, *104*(6), 2953–2965. https://doi.org/10.1785/0120140087

Liu, P., Archuleta, R. J., & Hartzell, S. H. (2006). Prediction of broadband ground-motion time histories: Hybrid low/high- frequency method with correlated random source parameters. *Bulletin of the Seismological Society of America*, *96*(6), 2118–2130. https://doi.org/10.1785/0120060036

Lyakhovsky, V., Ben-Zion, Y., Ilchev, A., & Mendecki, A. (2016). Dynamic rupture in a damage-breakage rheology model. *Geophysical Journal International*, *206*(2), 1126–1143. https://doi.org/10.1093/gji/ggw183

Meng, H., & Ben-Zion, Y. (2018a). Characteristics of airplanes and helicopters recorded by a dense seismic Array near Anza California. *Journal of Geophysical Research: Solid Earth*, *123*, 4783–4797. https://doi.org/10.1029/2017JB015240

Meng, H., & Ben-Zion, Y. (2018b). Detection of small earthquakes with dense array data: Example from the San Jacinto fault zone, southern California. *Geophysical Journal International*, *212*(1), 442–457. https://doi.org/10.1093/gji/ggx404

Mori, J., & Hartzell, S. (1990). Source inversion of the 1988 Upland, California, earthquake: Determination of a fault plane for a small event. *Bulletin of the Seismological Society of America*, *80*(3), 507–518.

Obara, K. (2002). Nonvolcanic deep tremor associated with subduction in Southwest Japan. *Science*, *296*(5573), 1679–1681. https://doi.org/10.1126/science.1070378

Ou, G. B. (2008). Seismological studies for tensile faults. *Terrestrial, Atmospheric and Oceanic Sciences*, *19*(5), 463–471. https://doi.org/10.3319/TAO.2008.19.5.463(T)1

Peterson, J. (1993). Observation and modelling of seismic background noise, U.S. Geol. Surv. Tech. Rept.

Pitarka, A., Somerville, P., Fukushima, Y., Uetake, T., & Irikura, K. (2000). Simulation of near-fault strong-ground motion using hybrid Green's functions. *Bulletin of the Seismological Society of America*, *90*(3), 566–586. https://doi.org/10.1785/0119990108

Riahi, N., & Gerstoft, P. (2015). The seismic traffic footprint: Tracking trains, aircraft, and cars seismically. *Geophysical Research Letters*, *42*, 2674–2681. https://doi.org/10.1002/2015GL063558

Ross, Z. E., Ben-Zion Y., Zhu L. (2015). Isotropic source terms of San Jacinto fault zone earthquakes based on waveform inversions with a generalized CAP method. *Geophysical Journal International*, *200*(2), 1269–1280. https://doi.org/10.1093/gji/ggu460

Ross, Z. E., Trugman, D. T., Hauksson, E., & Shearer, P. M. (2019). Searching for hidden earthquakes in Southern California. *Science*, *364*(6442), 767–771. https://doi.org/10.1126/science.aaw6888

Sato, T., & Hirasawa, T. (1973). Body wave spectra from propagating shear cracks. *Journal of Physics of the Earth*, *21*(4), 415–431. https://doi.org/10.4294/jpe1952.21.415

Shaw, B. E. (2013). Earthquake surface slip-length data is fit by constant stress drop and is useful for seismic hazard analysis. *Bulletin of the Seismological Society of America*, *103*(2A), 876–893. https://doi.org/10.1785/0120110258

Shelly, D. R., Beroza, G. C., & Ide, S. (2007). Non-volcanic tremor and low-frequency earthquake swarms. *Nature*, *446*(7133), 305–307. https://doi.org/10.1038/nature05666

Stierle, E., Bohnhoff, M., & Vavryčuk, V. (2014). Resolution of non-double-couple components in the seismic moment tensor using regional networks—II: Application to aftershocks of the 1999 Mw 7.4 Izmit earthquake. *Geophysical Journal International*, *196*(3), 1878–1888. https://doi.org/10.1093/gji/ggt503

Uchide, T., & Ide, S. (2010). Scaling of earthquake rupture growth in the Parkfield area: Self-similar growth and suppression by the finite seismogenic layer. *Journal of Geophysical Research*, *115*, B11302. https://doi.org/10.1029/2009JB007122

Yang, W., Hauksson, E., & Shearer, P. M. (2012). Computing a large refined catalog of focal mechanisms for Southern California (1981–2010): Temporal stability of the style of faulting. *Bulletin of the Seismological Society of America*, *102*(3), 1179–1194. https://doi.org/10.1785/0120110311

Yenier, E., & Atkinson, G. M. (2015). Regionally adjustable generic ground-motion prediction equation based on equivalent point-source simulations: Application to central and eastern North America. *Bulletin of the Seismological Society of America*, *105*(4), 1989–2009. https://doi.org/10.1785/0120140332

Zheng, G., & Rice, J. R. (1998). Conditions under which velocity-weakening friction allows a self-healing versus a cracklike mode of rupture. *Bulletin of the Seismological Society of America*, *88*(6), 1466–1483.